An experimental investigation into influences of build orientation and specimen thickness on quasi-static and dynamic mechanical responses of Selective Laser Melting 316L Stainless Steel

Hugo Carassus, Jean-Dominique Guerin, Hervé Morvan, Grégory Haugou, Tarik Sadat, Sandra Guerard, Eric Markiewicz

An experimental investigation into influences of build orientation and specimen thickness on quasi-static and dynamic mechanical responses of Selective Laser Melting 316L Stainless Steel

H. Carassus [a, c], J.D. Guérin [b,*], H. Morvan [a], G. Haugou [a] T. Sadat [a], S. Guérard [c], E. Markiewicz [a]

[a] *Univ. Polytechnique Hauts-de-France, CNRS, UMR 8201-LAMIH, F-59313 Valenciennes, France*
[b] *INSA Hauts-de-France, F-59313 Valenciennes, France*
[c] *Arts et Métiers ParisTech, I2M, CNRS UMR 5295, F-33405 Talence, France*

*** Corresponding author: Jean-Dominique.Guerin@uphf.fr**
Keywords: Additive manufacturing, stainless steel, dynamic behavior, SEM analysis

Additive Layer Manufacturing (ALM) processes like Selective Laser Melting (SLM) enable the conception of complex designs with a high precision and equal or enhanced mechanical properties compared to Conventionally Manufactured (CM) structures. Nevertheless, this process, which consists in melting metallic powders layer by layer with a laser beam, greatly influences the microstructure and therefore the mechanical properties. While some studies have considered the effects of the thickness and/or the building direction of 316L Stainless Steel (SS) specimens produced by SLM on the quasi-static mechanical behavior, the strain rate effect for crash or impact applications on these two parameters has not been fully investigated. To complete the actual knowledge, the present work proposes to analyze the mechanical behavior of 316L SS tensile specimens produced by SLM with different build orientations (0°, 45° and 90°) and thicknesses (0.5, 0.75, 1 mm) and submitted to dynamic loadings at various strain rates up to 10^3 s^{-1}. In addition, the microstructure and the fracture surfaces are analyzed to give a more detailed comprehension of the mechanical tests. It results that the SLM 316L SS achieves better Yield Stress (YS), similar Ultimate Tensile Stress (UTS) and equal or lower failure strain compared to the CM material. This is mainly a result of microstructure refinement. Anisotropy is observed at the macroscopic level with higher tensile stress and lower failure strain for horizontal specimens, which is explained by the different shapes, orientation and size of the grains at the microscopic level. The mechanical properties greatly decrease as the thickness reduces from 1 to 0.5 mm, by 14% for the YS and 16% for the UTS for a quasi-static loading. A minimum thickness of 0.75 mm is advised to at least recover the mechanical properties of the CM 316L SS. A positive strain rate sensitivity, higher than the CM material, is observed for all configurations, with the exception of 0.5 mm thickness. For strain rates ranging from to 10^{-3} to 10^3 s^{-1}, there is an increase of 20% of the UTS. The material anisotropy is not affected by the strain rate sensitivity whereas the latter increases with the thickness.

Nomenclature

P	[W]	**Laser power (SLM)**
s	[m·s^{-1}]	**Scan speed**
h	[m]	**Hatching space**
l	[m]	**Layer thickness**
E_v	[J·m^{-3}]	**Volumetric Energy Density (VED)**
$\varepsilon_i, \varepsilon_r, \varepsilon_t$	[1]	**Elastic strain of the incident, reflected and transmitted pulses**
$\dot{\varepsilon}$	[s^{-1}]	**Equivalent plastic strain rate**
m	[1]	**Strain rate sensitivity parameter**
r	[1]	**Lankford ratio**

Abbreviations

ALM	**Additive Layer Manufacturing**
SLM	**Selective Laser Melting**
CM	**Conventionally Manufactured**
SS	**Stainless Steel**
MAM	**Metallic Additive Manufacturing**
YS	**Yield Stress**
UTS	**Ultimate Tensile Stress**
VED	**Volumetric Energy Density**
BD	**Building direction**
SD	**Scanning direction**
TD	**Tensile direction**
TrD	**Transverse direction**

1. Introduction

Metallic Additive Manufacturing (MAM) processes like Selective Laser Melting (SLM) have attracted more and more attention in recent scientific research and industry over the past decade. They allow to design complex and innovative structures by creating near-net shaped parts without any expensive machining [1–3]. SLM is a power bed fusion process with a layer-by-layer build-up method which allows to reach the microscopic scale, enabling the production of a monolithic design whereas other conventional process would not be adapted. Metallic powder particles are melted together by a laser following a scanning path strategy. This generates high cooling rates during the solidification which leads to a really fine microstructure with residual stresses [4]. As a result, the mechanical behavior of SLM parts differs from those of conventional processes as casting or machining [5].

Cellular materials with complex periodic unit cells benefit from these emerging technologies. They can now be easily optimized and built in order to satisfy the specific needs of industrial applications (energy, defense and aerospace) such as reduction in weight and/or enhanced energy absorbing capabilities for crash or impact applications [6–9]. Thus, in order to use cellular materials made by SLM for functional applications, it is necessary to understand the influence of key process parameters on the mechanical behavior, such as the strain rate sensitivity of the constitutive material produced by SLM, the building orientation or the part thickness.

A wide range of alloys can be considered with the SLM process, the best-known being Titanium Ti6Al4V [2], Aluminum AlSi10Mg [10] or 316L Stainless Steel (SS) [11]. For energy absorbing applications, 316L SS is considered among the best choice for its high strength-ductility combination [12]. This ferrous alloy contains only austenite phase and is popular due to its high corrosion resistance [13]. In the present study, our attention is focused on this specific alloy. The mechanical properties of SLM 316L SS parts such as Yield Stress (YS) or Ultimate Tensile Stress (UTS) are higher or equivalent to those of Conventional Manufactured (CM) parts [5,14]. It is explained by different microstructure characteristics such as cellular dendritic structure or grain morphology [4,15]. However, there are divergent results concerning the ductility of SLM parts. In some cases, an increase of the ductility compared to CM 316L SS is observed [16,17] whereas other works noticed the opposite [5,11]. This discrepancy is indicative of a large scatter in the literature of MAM that is also significant on the YS with values ranging from 406 - 649 MPa and on the UTS with values ranging from 509 - 760 MPa [4,18,19]. It can be explained by considering the multiplicity of process parameters combinations. Roach et al. [20] even shown that variations in mechanical properties are possible for samples printed simultaneously with the same process parameters on the same machine.

Most of the published research dealing on the strain rate sensitivity of 316L SS produced by SLM has been investigated on tensile specimens built parallel to the building direction up to strain rate of 1 s^{-1} [21–23]. Only Li et al. [5] have carried out tensile tests in the range of 10^{-3} to 10^{2} s^{-1}. The latter concluded to a positive strain rate sensitivity with an increase of the YS by 26%. Thus, the dynamic response of the 316L SS SLM remains relatively undefined.

The specific microstructure induced by SLM has been recognized to be responsible for anisotropic mechanical properties [5,12,24]. Grains, subgrain structures, interface between layers, texture and deformation mechanisms are the main reasons mentioned explaining this dependence to the building orientation. In the literature, specimens built vertically (along the building direction) have higher flow stress but lower failure strain than horizontally built samples. Although the trend is accepted for these two build orientations, it remains uncertain for intermediate angles in between. Either there is a decreasing trend from horizontally built samples to those vertically built in terms of YS and UTS, or YS and UTS are highest for angles in between [25]. Moreover, these published works are limited to quasi-static loading tensile tests in the case of SLM 316L SS. Maconachie et al. [10] suggested, for Aluminum alloy AlSi10Mg, that in terms of tensile strength, there was no significant difference between building directions of 0° - 45° - 90° in quasi-static and dynamic loadings.

For specimens produced by SLM process, the microstructure is influenced by many factors such as the processing parameters, the build orientation but also by the parts thickness [20,26,27]. It has been shown that the latter can affect the thermal history during the fabrication and consequently the mechanical behavior. Several works [28–31] have demonstrated that the SLM process is able to produce micro-struts with a diameter close to 200 µm built with a single spot exposure layer by layer. Gümrük et al. [29] pointed out a standard deviation higher than 10% in the measured diameter of the struts with heavy imperfections and structural disorders, resulting in lower mechanical properties compared to CM 316L SS. In the case of SLM 316L SS, a minimum thickness of 0.5 mm is advised to have a reasonable geometric accuracy [8]. Only a few studies [8,20,27,32] focused on the influence of the specimen thickness near to this minimum value of 0.5 mm on the microstructure and the mechanical properties. Leicht et al. [32] revealed that plate specimens with a thickness of 0.4 mm had an almost random texture with uniform grains whereas higher thicknesses displayed large elongated grains with a predominant orientation parallel to the building orientation. Roach et al. [20] observed an increase of the effective stiffness by 50% when increasing the specimen thickness from 0.4 to 6.25 mm. Tancogne-Dejean et al. [8] noticed the same tendency with an increase by nearly 50% of the YS when increasing the diameter of cylindrical specimens from 0.8 to 8 mm. To the best of our knowledge, all studies were done on quasi-static loading tensile tests in the case of SLM 316L SS and the influence of the dynamic loading on the mechanical properties for several thicknesses has not been investigated.

Thus, according to the state of the art, this paper proposes as novelty to study the effect of the build orientation and specimen thickness for strain rates ranging from 10^{-3} to $10^{1}\ \mathrm{s}^{-1}$ on the mechanical properties of 316L SS SLM specimens. Three thicknesses (0.5 - 0.75 – 1 mm) and three building orientations (0° - 45° - 90°) are considered. The strain rate sensitivity for higher ranges up to $10^{3}\ \mathrm{s}^{-1}$ is investigated on vertically build specimens using Split Hopkinson Tensile Bar (SHTB) setup. Microstructural analysis with optical and scanning electron microscopy are also performed to give a better understanding of the macroscopic mechanical response of SLM 316L SS specimens. In addition to contribute to the knowledge of the SLM process, the parameters investigated in this study are also relevant to ensure a reliable design of complex cellular materials manufactured by SLM and explain their mechanical response under dynamic loading for crash or impact applications.

2. Materials and methods

a. Materials and SLM process

The SLM 316L SS specimens examined in this study were fabricated using a SLM 280 machine from SLM-Solution. The nominal chemical composition of the pre-alloyed 316L SS powder with a particle size ranging from 15 to 45 µm and a spherical shape is given in **Table 1**. The processing parameters used to prepare specimens were: laser power P = 200 W, scanning speed s = 800 $\mathrm{mm \cdot s^{-1}}$, hatch spacing h = 120 µm, layer thickness l = 30 µm and a single scan layer meandering scan strategy was chosen (**Fig. 1**). These four parameters were the standard parameters set by the manufacturer to produce specimens with near full density and calculate the Volumetric Energy Density (VED) E_V, defined as followed:

$$E_V = \frac{P}{s * h * l} \tag{1}$$

With the parameters presented above, E_V corresponds to a value of 69 $\mathrm{J \cdot mm^{-3}}$. Liverani et al. [33], with the same scan strategy, found an optimal range of VED of 49-79 $\mathrm{J \cdot mm^{-3}}$ where the number of porosities in this range was minimized, ensuring a reliable mechanical behavior.

Table 1. Chemical composition (in weight total percentage) of 316L SS powder.

Fe	Cr	Ni	Mo	Mn	Si	N	C	P, S

67-69	16-18	10-14	2-3	2	0.75	< 0.1	< 0.03	< 0.045

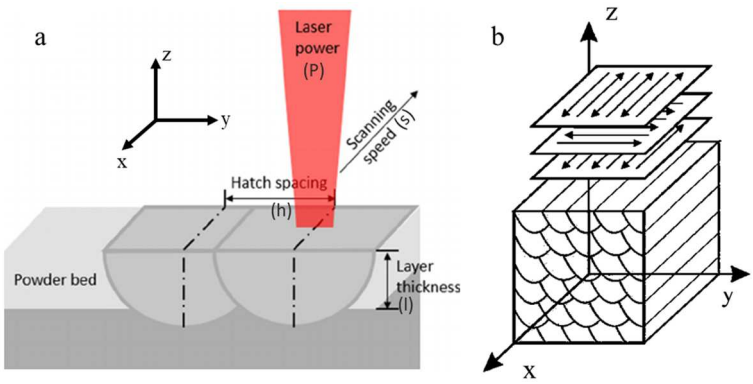

Fig. 1. Scheme relative to: (a) the SLM process with main parameters, (b) representation of the scan strategy pattern with Z as the Building Direction (BD) and X the Scanning Direction (SD).

The build plate with all the specimens organized in six configurations is shown in **Fig. 2a**. In order to distinguish them, they are named according to their Building Direction (BD) and thickness. For example, a dog bone specimen with 1 mm thickness and printed horizontally, 0° - along the Scanning Direction (SD), is named Bd0_t1. All the specimens are designed to study the strain rate sensitivity considering a significant strain rate gap. A special attention is paid to the high strain rate range knowing its influence on strain hardening. The geometry of the specimens for the Split Hopkinson Tension Bars (SHTB), presented in **Fig. 2**b, has been designed especially for this experimentation to reach the targeted strain rate. For the moderate and quasi-static strain rate ranges specimens (**Fig. 2**c), gage length and width of specimens have been chosen to cover a wide range of strain rates (close to two decades). No machining was applied to the samples, except to remove them from the build plate. In this study, it is a will to consider the edge effects on the specimens as it can be the case on the structures produced by SLM for energy absorption applications, for example. 1 mm and 1.5 mm thickness specimens were sandblasted, then thermally treated for two hours at 1095°C and water quenched. Due to thin geometry, 0.5 - 0.75 mm thickness samples were not post treated in order to ensure their structural integrity. The possible differences between post-treated and not post-treated specimens will be analyzed in the discussion section.

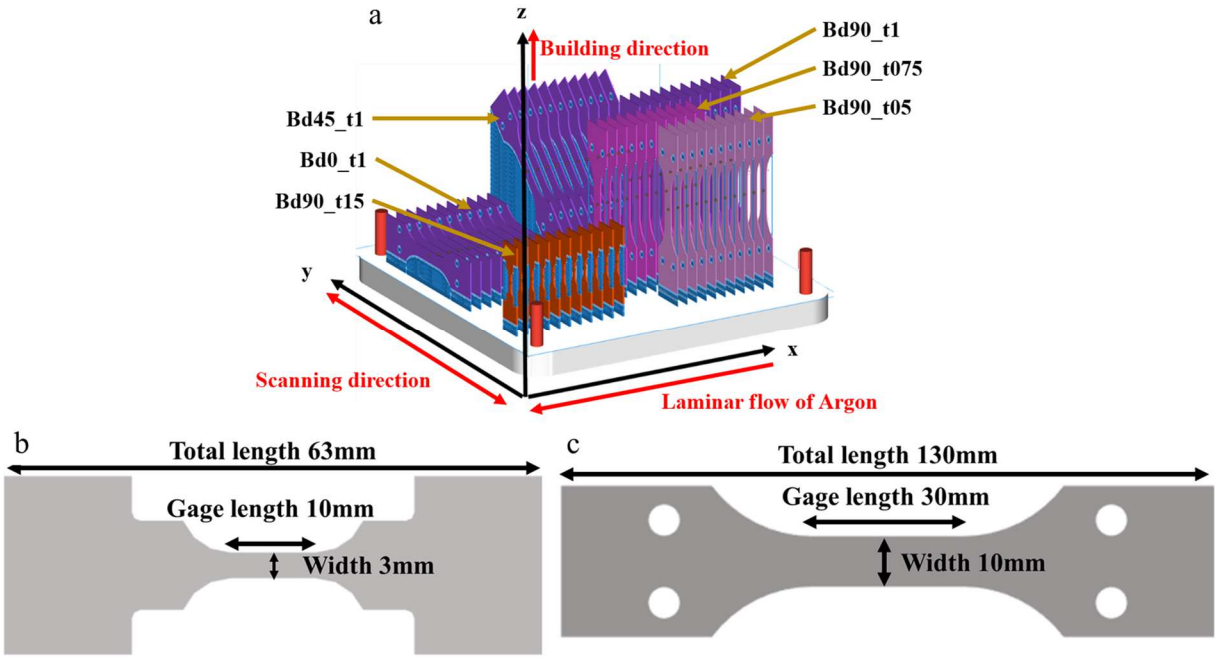

Fig. 2. Tensile specimens: (a) build plate and spatial localization of all dog bone specimens; Computed Aided Design (CAD) designs of specimens with (b) 1.5 mm thickness specific for the SHTB and (c) 0.5 - 0.75 - 1 mm thickness.

b. Microstructure analysis

To study the microstructure, two cross-sections in the center of the specimens are considered (**Fig. 3**). The grain morphology is observed along the Tensile Direction (TD), ZX-plane for Bd90 and XY-plane for Bd0. The defects and laser tracks are also studied along the TD but also perpendicularly to that direction, XY-plane for Bd90 and ZX-plane for Bd0. The polishing is realized in four steps, with SiC papers from 220 to 1 µm, to achieve a mirror surface. Then samples are etched with Villela solution for 30 seconds to reveal the microstructure and observe the laser scans, melt pools and porosities on the optical microscope Nikon Epiphot 200 and on the Scanning Electron Microscope (SEM). Electron BackScatter Diffraction (EBSD) is performed using JOEL JSM-7100F Field Emission Scanning Electron Microscope and OXFORD EBSD detector to examine the grain shape and orientation along the TD. For EBSD analysis, after being polished to obtain a mirror surface, samples are etched with Struers OP-S Chem solution for two minutes and then electro-polishing (Struers LectroPol-5) is carried out using a standard solution A2. A voltage of 15 kV is considered, a step size of 0.4 µm is fixed, and an area of 1000*1000 µm² for 1 mm thickness specimens and of 500*1500 µm² for 0.75 - 0.5 mm thickness specimens are chosen. EBSD data are analyzed using the AZTec (UK) software from OXFORD instruments. SEM images of post-mortem specimens are also captured to observe the presence of dimples and fracture surfaces.

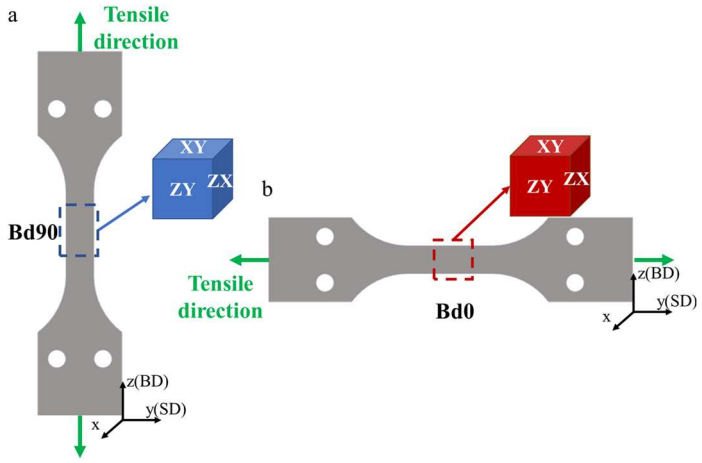

Fig. 3. Schematic representation of (a) Bd90 and (b) Bd0 specimens showing the different cross-sections along the BD, the SD and the Tensile Direction (TD).

c. Measurements and mechanical tests

To control the good fabricability of all tensile specimens, the density is measured for each one using Archimedes's method using water, and as no machining is realized after removal, the dimensions are verified using a caliper with a resolution of 0.01 mm. Three measurements at different locations in the gage section of the gage length and the thickness of each sample are done and an average value is calculated per configuration in order to compare with the design values.

Vickers hardness tests are carried out to assess if there is a difference at the grain scale between the various configurations. Three measurements at three different locations per polished specimen are realized with a Vickers indenter at a load of 100 g for 15 s on a Future-Tech microhardness tester, according to ASTM E384-17 [34] standard.

Quasi-static tensile tests are done on a MTS Sintech, an electromechanical testing machine, with a 30 kN load cell at a loading rate of 1 $mm \cdot min^{-1}$ (0.00057 s^{-1}). Images of the tensile tests are taken with a digital camera Manta Allied Vision with an acquisition frequency of 1Hz and a spatial resolution of 15 µm. The increase of the loading rate to 2 $mm \cdot s^{-1}$(0.067 s^{-1}) and 240 $mm \cdot s^{-1}$(8 s^{-1}), is realized with an Instron VHS, a servohydrolic testing machine, with a 30 kN load cell. A Fastcam Photron APX RS camera is used for 0.067 - 8 s^{-1} strain rates with acquisition frequencies of 50 – 7500 Hz respectively and a spatial resolution of 157 µm. Load and image acquisitions are simultaneously triggered by a digital oscilloscope Yokogawa DL750. Displacements and strains of the three lower strain rates are calculated by Digital Image Correlation using an intern MATLAB© script based on a black speckle on a white background spread on all the tensile test specimens.

SHTB are chosen to reach the two highest loading rates of 3 $m \cdot s^{-1}$ (300 s^{-1}) and 10 $m \cdot s^{-1}$ (1000 s^{-1}). The SHTB experimental setup, developed by the laboratory, is composed of a 7.5 m long incident bar and a 7 m long output bar, both with a diameter of 11 mm. These bars are made of maraging steel to generate high strength level. Strain gages are fixed on each bar to measure the elastic waves using a high-speed recorder (Yokogawa DL 850 - 4 channels up to 100 MHz). Before each test, the input bar is elastically pre-stretched to store the required amount of the incoming energy. When the pretension is dynamically released, a unidirectional tensile wave ε_i is generated and propagates in the direction of the specimen. This wave is separated into two complementary elastic waves: the transmitted impulse travels through the output bar and is called ε_t and the other part goes back through the incident bar and is mentioned as ε_r. The commonly used theory established by Kolsky is used to calculate the stress-strain data from the measurement collected by the three signals ε_i, ε_t and ε_r. Full details are given in [35].

Considering a repeatability of three specimens per tensile test and two specimens dedicated to the study of the microstructure, it represents a total of 63 samples. The test matrix of the six configurations with the associated strain rates is given in **Table 2**.

Table 2. Test matrix of the six configurations.

Name	Heat treatment and sand blasted	Tensile tests				
		0.00057 s^{-1}	0.067 s^{-1}	8 s^{-1}	300 s^{-1}	1000 s^{-1}
Bd0_t1	yes	3	3	3		
Bd45_t1		3	3	3		
Bd90_t1		3	3	3		
Bd90_t075	no	3	3	3		
Bd90_t05		3	3	3		
Bd90_t15	yes				3	3

3. Experimental results

The results of microstructural analysis, quasi-static, intermediate and dynamic tensile tests and fracture surfaces analysis are detailed in this section.

As the specimens are not machined after being removed of the build plate, it is important to estimate the geometrical accuracy of the SLM process. Average measurements of the gage length and the thickness for each configuration are presented in **Table 3**. It shows a good agreement in general with a difference with CAD below 3.1%, except for 0.5 mm thickness sample with a 7.4% difference. This could be expected because this value is tending toward the minimum feature size of the SLM process. An average relative density is also determined for each configuration. Only samples with a 0.5 mm thickness have a relative density lower to 99%, which is the minimum recommended to achieve good mechanical properties [22,36]. It demonstrates the actual limitations of the SLM process to produce very thin parts.

Table 3. Measurements of width, thickness and relative density of samples compared with CAD files.

Configuration	Width (mm)	Difference with CAD (%)	Thickness (mm)	Difference with CAD (%)	Relative density (%)
Bd0_t1	10.25	2.5	0.99	1.9	99.5
Bd45_t1	10	0.3	1.03	2.6	99.9
Bd90_t1	9.83	1.7	0.99	0.9	99.6
Bd90_t075	9.83	1.7	0.75	0.9	99.7
Bd90_t05	9.87	1.3	0.54	7.4	98.5
Bd90_t15	2.93	2.3	1.45	3.1	99.9

a. Microstructure

The specificities induced by the SLM process are observed on the microstructure of the specimens at multiple scales.

The microstructures observed on etched samples in the XY-plane in **Fig. 4**a-c show the scanning strategy with parallel laser paths, more prominently on edges where remelting is less important than in the center. In the ZX-plane (**Fig. 4**d-f), the stacking of layers with semicircular and elongated melt pools perpendicularly to the BD can be observed. The shape is less discernible at the center than on the edges, always influenced by remelting.

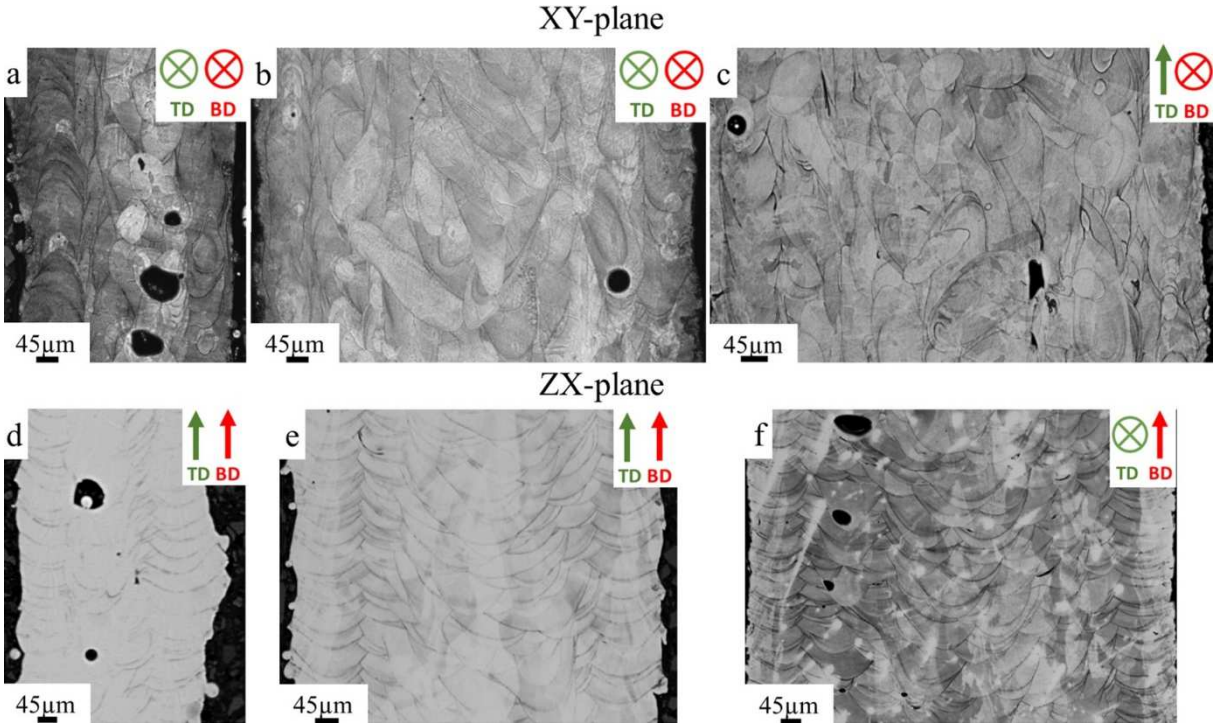

Fig. 4. Optical micrographs after etching of (a,d) Bd90_t05, (b,e) Bd90_t1 and (c,f) Bd0_t1 in the XY-plane (SD) and ZX-plane (BD).

Considering the optical micrographs, a larger number of defects, in number and size, can be seen on Bd90_t05 compared to other configurations. These defects are unmelted particles of powder which were pulled out from the sample during the polishing. The spherical shape and the similar size, 15 to 45 µm, confirm this statement. Three other types of defects have been observed for all configurations:

- Lack of fusion pores with irregular shapes at the boundaries between layers or melt pools (**Fig. 5**a). This is due to a low energy density causing a lack of fusion between layers or an insufficient recovery of two melt pools. It leads to lack of cohesion between layers [37,38].
- Gas induced porosity footprint is represented by spherical defects (**Fig. 5**a). It contains gas entrapped inside the powder particles during the powder atomization. It can also be caused by the entrapment of gas from the built chamber [39].
- Keyhole defects are observed on samples in ZX-plane (**Fig. 5**b). It is due to an excessive laser power or VED [40].

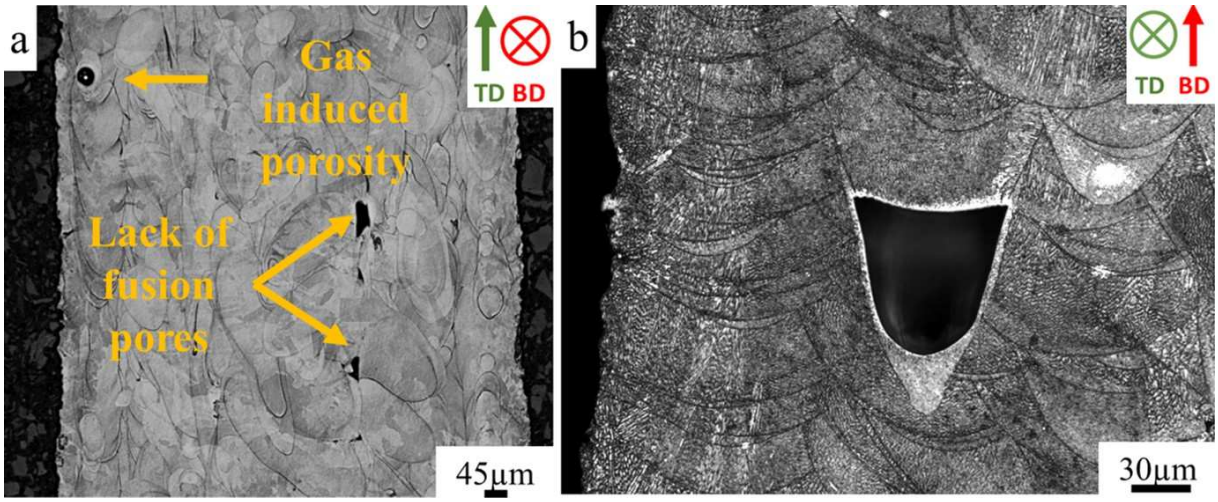

Fig. 5. Optical micrographs of (a) Bd0_t1 etched samples presenting lack of fusion pores and gas induced porosity in XY-plane, (b) Keyhole induced porosity in ZX-plane.

On **Fig. 6**a, SEM images present the fine cellular structure inside melt pools with a grain size in the range of 0.1 - 2 µm. The high-cooling rate, in the order of $10^4 - 10^6$ K · s^{-1}, generates non-equilibrium solidification conditions which cause this subgrain structure [41,42]. During the melting process, the dendritic structure is oriented along the maximal local thermal gradient, which can be different from the macroscopic one. It then leads to multiple orientations inside a melt pool. At higher magnification (**Fig. 6**b), coarser subgrain microstructure due to multiple melting can be observed [10].

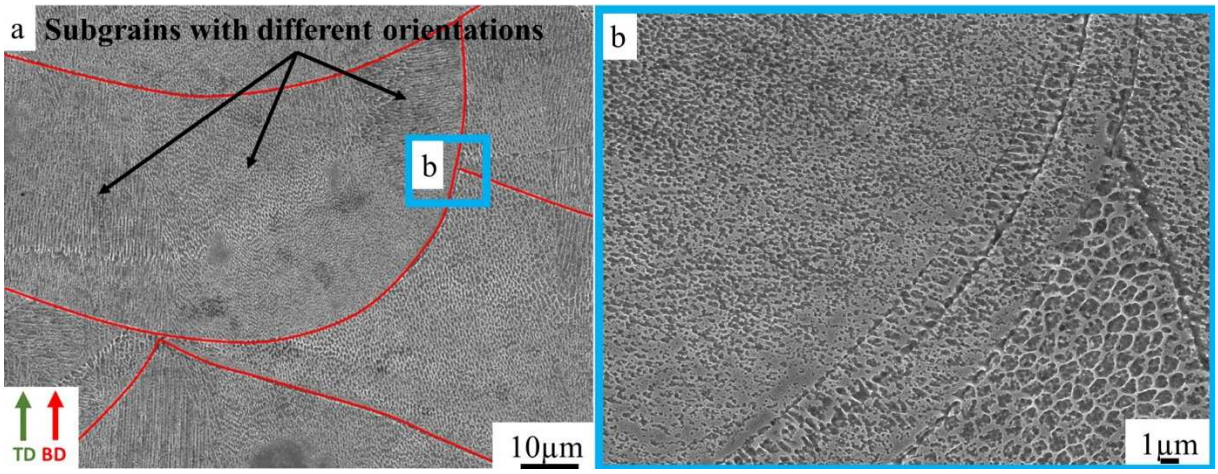

Fig. 6. (a) SEM images of Bd0_t1 sample in ZX-plane with melt pool boundaries highlighted in red, and (b) a higher magnification of the junction of melt pool boundaries.

EBSD orientation maps and Inverse pole figure maps (IPF) of vertically, diagonally and horizontally built specimens with 1 mm thickness are presented in **Fig. 7**a-c. Bd90_t1 contains large grains oriented toward the BD compared to Bd0_t1 with most of the grains being narrow and elongated perpendicularly to the TD. The solidification process, as presented in **Fig. 7**d, explains the shape and the orientation of the grains when considering the microstructure of Bd0_t1, as it is observed along the SD (XY-plane). On the edges of specimens, small grains can be found. As they are not subjected to multiple melting and cooling time is higher, the grain size is smaller [20]. Closer to the center of specimens, the microstructure is randomly distributed thanks to the remelting process and the influence of layers on the side and underneath. Clusters of small grains are present in horizontal specimens. According to Balit et al. [43], it is attributed to particular values of the solidification rate and the thermal gradient. They are located mostly near the solidification front. Bd45_t1 (**Fig. 7**b) shows a microstructure which is a blend of the two previous one with a grain size more homogenous and more equiaxed grains.

For all configurations, the grains spread over multiple melt pools, which is typical of epitaxial growth. This disposition is imposed by the maximal local thermal gradient and remelting of layers that dictate the same crystallographic orientation [12]. In the case of the SLM process, it is commonly observed [44,45]. The IPF associated to the EBSD maps reveal a <001> fiber texture for Bd90_t1 whereas two preferred crystallographic orientations of lower intensities, <001> and <101>, are discernible for Bd0_t1. As the 316L SS shows an FCC structure, the evolution of a <001> texture is favored [27,46], as it is noticed for the two previous configurations. The additional <101> texture observed for Bd0_t1 is induced by the solidification direction (**Fig. 7**d). In the case of Bd45_t1, there is no preferred crystallographic orientation. As the melt pool shape is directly linked to the texture development [47], it explains the absence of preferred orientation for Bd45_t1 which has a homogeneous grain structure. Thus, the different melt pool shapes observed previously for the three BD are mainly responsible for the distinct preferred crystallographic orientations.

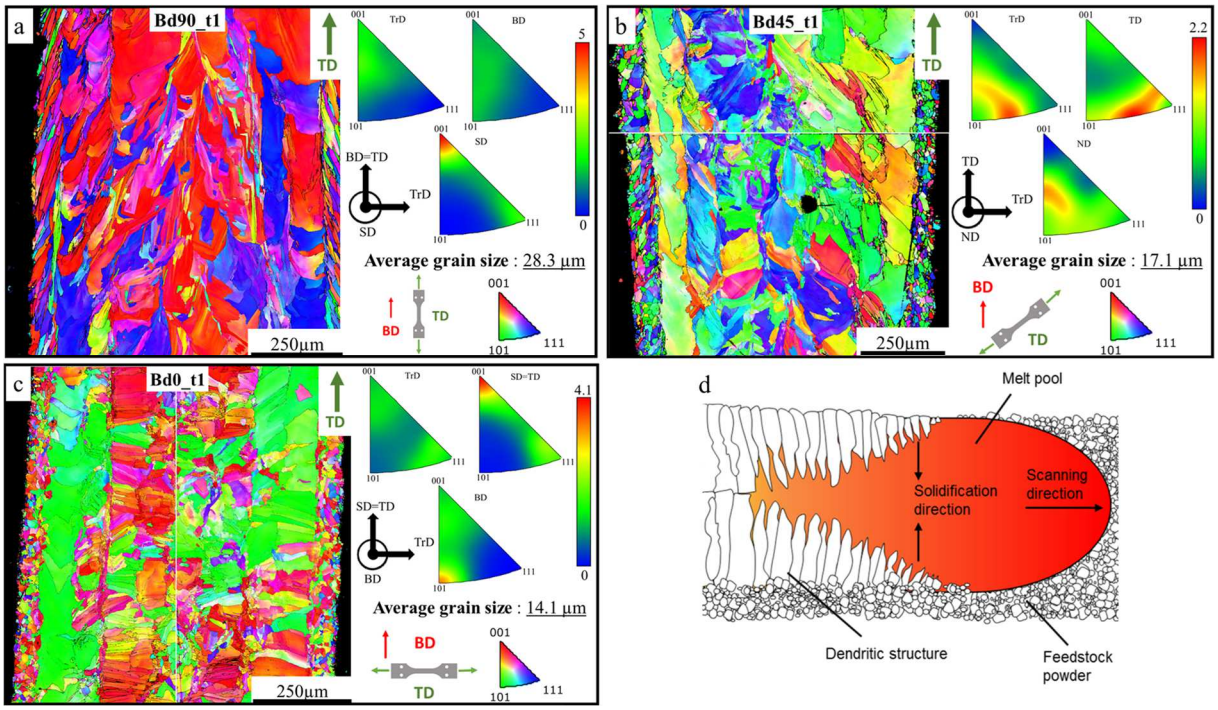

Fig. 7. Influence of the BD on the microstructure of 316L SS SLM specimens: EBSD maps and the corresponding inverse pole figures (IPF) with the average grain size of (a) Bd90_t1, (b) Bd45_t1, (c) Bd0_t1, the microstructures are shown along the TD relative to the BD, the SD, and the Transverse Direction (TrD) ; (d) scheme of the SLM solidification process.

The microstructures of the specimens with a thickness of 0.5 and 0.75 mm in **Fig. 8** present similar elongated grains oriented along the BD than Bd90_t1 and also a <001> fiber texture. The intensity of the texture and the grain size are supposed to increase with the thickness due to the variation of thermal gradients and cooling rates [12,32]. This statement is true with the exception of the texture of Bd90_t1. The latter was thermally treated and as suggest the authors [48,49], the heat treatment reduces the pronounced texture of SLM 316L SS. Thus, a higher intensity of texture than Bd90_t075 can be expected without a heat treatment for Bd90_t1. The EBSD map of Bd90_t05 in **Fig. 8**b also points out a higher density of defects, leading to a weaker cohesion between the layers and a relative density inferior to 99%, as mentioned previously.

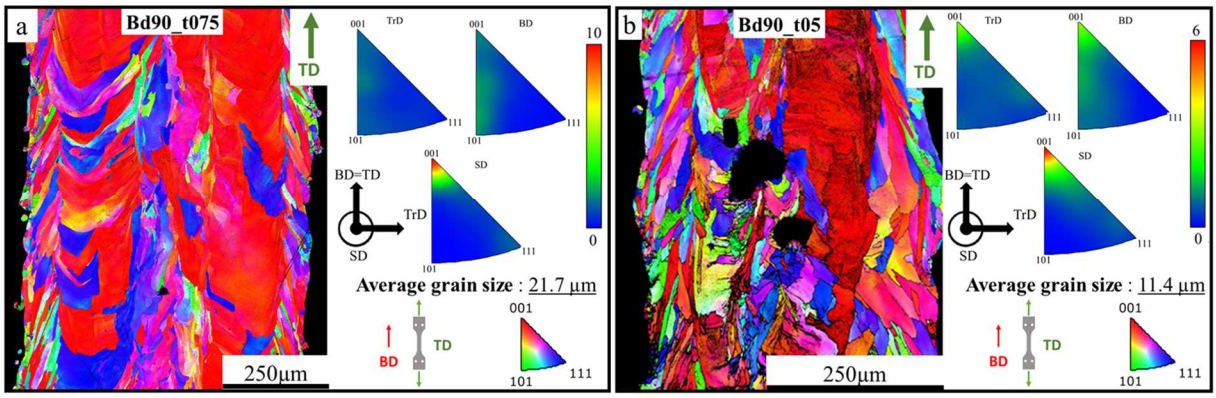

Fig. 8. Influence of the thickness on the microstructure of 316L SS SLM specimens: EBSD maps and the corresponding inverse pole figures (IPF) with the average grain size of (a) Bd90_t075, (b) Bd90_t05. The microstructures are shown along the TD relative to the BD, the SD, and the Transverse Direction (TrD).

b. Fracture surfaces

SEM images of the fracture surfaces of specimens are presented in **Fig. 9**. All six configurations have dimple-like features on fracture surfaces which are characteristic of ductile fracture behavior [23]. With the dimple size being smaller than 1 µm, it can be considered that the fracture behavior is transgranular and is not controlled by the grain size [22,27]. The unmelted particles are observed on surfaces of specimens but there were also trapped inside porosities during the melting process. Throughout the tensile tests, these defects cause the apparition of microcracks, which results in macroscopic cracks [50]. Theses defects discussed previously are responsible for not fully dense samples. Maconachie et al. [10] observed that crack propagation is done through or along melt pool boundaries, which means that it is the orientation of the melt pools and not the grains that imposes the fracture behavior.

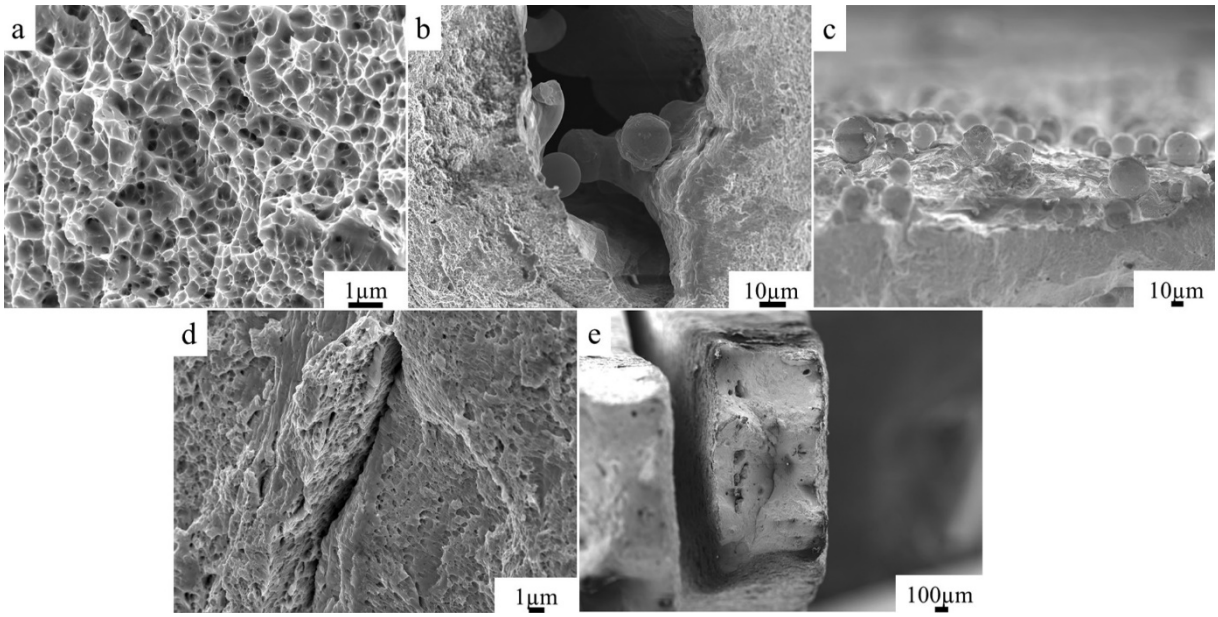

Fig. 9. SEM images of post-mortem specimens presenting (a) dimples, (b) unmelted particles inside porosities and (c) on the free edges, (d) microscopic (e) and macroscopic cracks.

c. Mechanical properties

The average Vickers Hardness of the three indenting locations with the corresponding standard deviation are presented for each configuration in **Fig. 10**a. Most values fall between 230 - 240 HV with an average value of 235±9 HV, which corresponds to results found by other researchers on samples made from the same material and using SLM [18,20,51]. It is also higher than the CM 316L SS, which fall in the range of 215 - 225 HV [52], because of the sugbrain microstructure and a higher dislocation density (10^{15} m^{-3}

for SLM versus 10^{10} m^{-3} for CM) [42]. Measurements are realized at several locations (top, middle, bottom) of polished samples and also on etched samples to observe if the indentation is different inside a melt pool or along a boundary (**Fig. 10**b). Results are homogeneous over the samples for all configurations. Thus, at the microscopic scale, this study shows in the same time that there is no significant influence of the BD and thickness on hardness values.

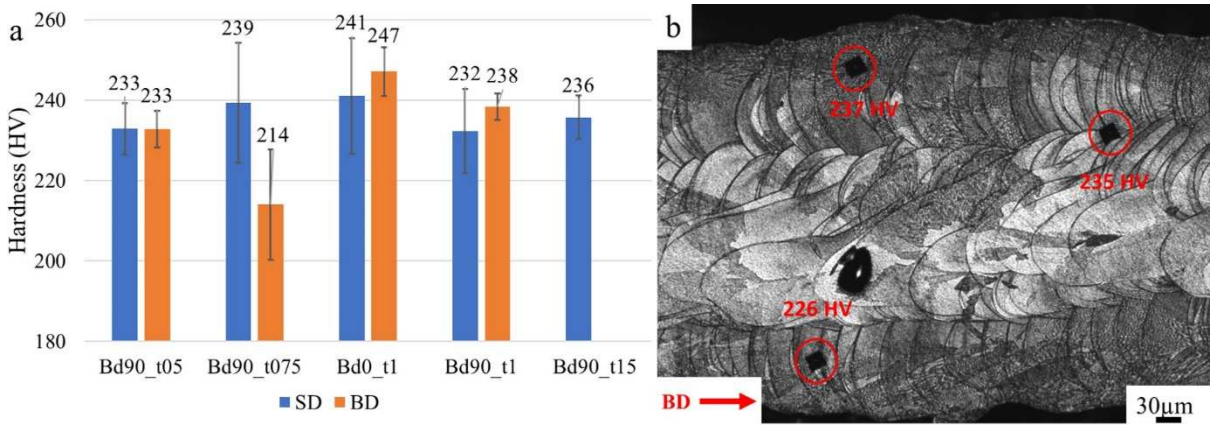

Fig. 10. (a) Vickers Hardness of the samples along the BD and the SD and (b) optical micrograph showing location of indentations on Bd90_t05 etched sample along the BD.

Concerning the material mechanical behavior, three repetitive tensile tests have been realized for each configuration. Mean true stress-strain curves of the tensile tests for all configurations at various strain rates are shown in **Fig. 11**. In the case of the SHTB tests, a smoothing with a span of 10% of the total number of data points is applied to the stress strain curves to remove noise from the acquired signal and to reduce effects of stress wave propagation. Mean engineering mechanical parameters $\sigma_{0.05}$ (stress for a 0.05 strain), UTS and failure strain ε_f with associated standard deviations are extracted from engineering stress-strain plots following the ASTM E8/E8M [53] procedure. The results are presented in **Fig. 12**. The 0.2% offset YS is measured on quasi-static tensile tests based on the usual Young Modulus consideration. The values for the three orientations are presented in **Table 4** and values for Bd90_t05 and Bd90_t075 are respectively 393±6 MPa and 453±5 MPa. Bd0_t1 specimens exhibit a higher $\sigma_{0.05}$ and UTS than other configurations at the three slower strain rates. This trend was also observed in other published works [43,54]. Bd90_t05 specimens exhibit by far the lowest $\sigma_{0.05}$ and UTS among the five configurations. These mechanical parameters increase along with the strain rate, with an increase of 24% of $\sigma_{0.05}$ and 20 % of UTS between strain rates of 10^{-3} to 10^{3} s^{-1} for vertical specimens. Failure strain of horizontal specimens is reduced by a factor of about two compared to other configurations. The latter does not show a clear trend with the increase of the strain rate. **Table 4** presents a comparison for YS, UTS and ε_f between results of the present work and results of previous published works. They appear consistent considering the wide dispersion of the results found in the literature. The comparison with the CM material and the associated mechanical requirements of the ASTM A240/A240M [55] shows that mechanical properties the SLM 316L SS are above the standard values and outperform the latter, except for Bd90_t05 and for failure strain of Bd0_t1.

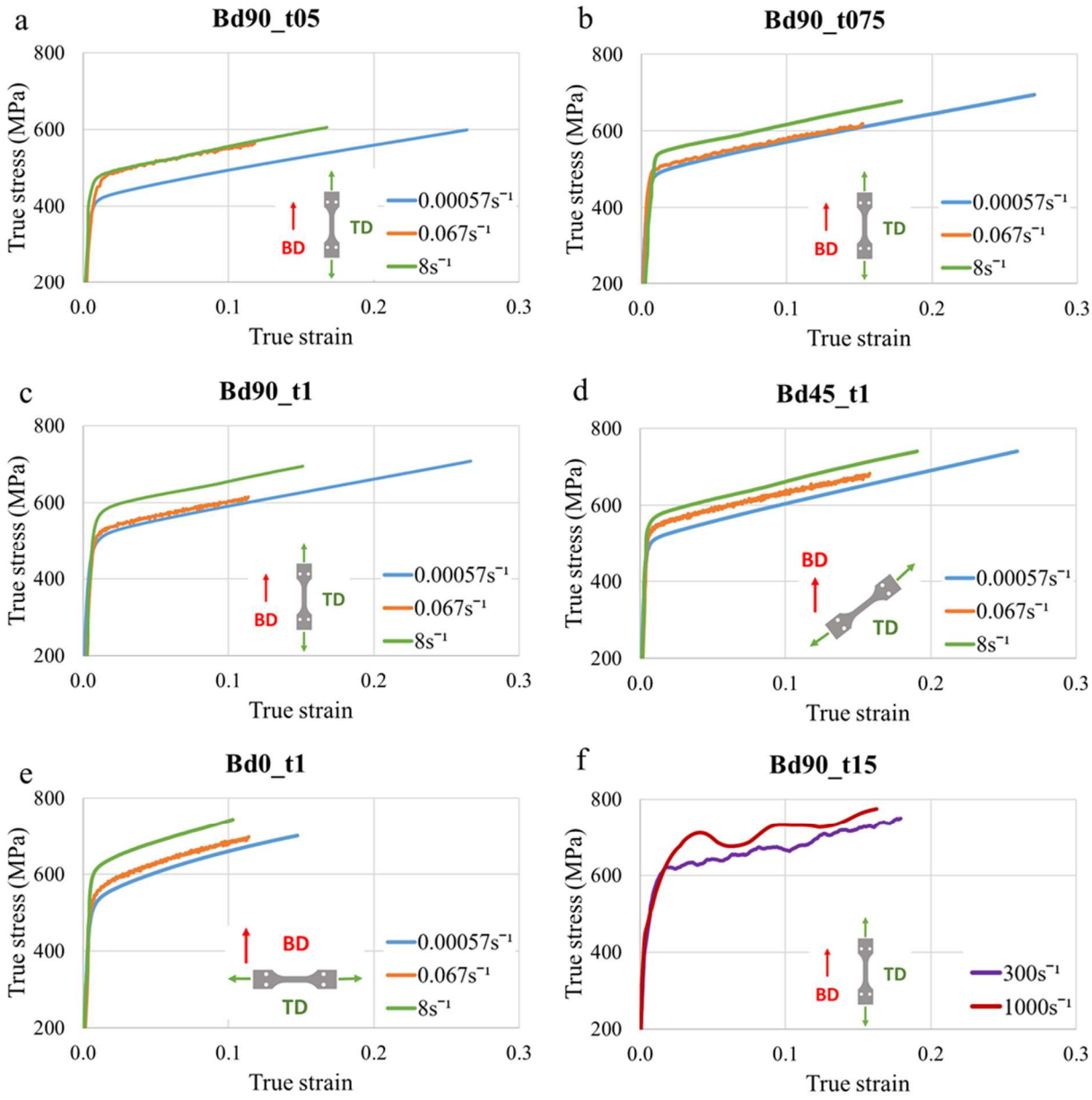

Fig. 11. True stress-strain curves of all configurations at strain rates of (a-e) 0.00057 to 8 s^{-1} and (f) Bd90_t15 at strain rates of 300 and 1000 s^{-1}.

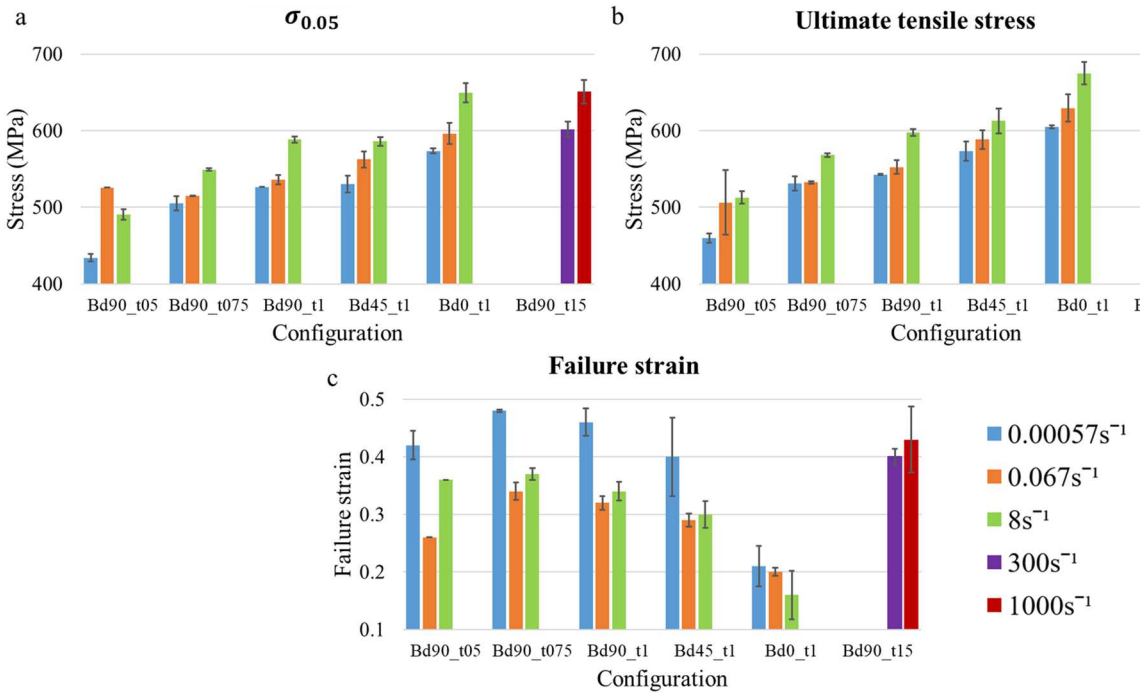

Fig. 12. Engineering mechanical parameters (a) $\sigma_{0.05}$, (b) UTS and (c) failure strain for all configurations and various strain rates with the associated standard deviation.

Table 4. Comparison of engineering mechanical parameters between this work, literature [4,5,11,17–19,25,56–59] and the norm ASTM A240/A240M [55] for a quasi-static loading.

Mechanical parameters	**YS (MPa)**			**UTS (MPa)**			**Failure strain (%)**		
Build orientation	**Bd90**	**Bd45**	**Bd0**	**Bd90**	**Bd45**	**Bd0**	**Bd90**	**Bd45**	**Bd0**
Literature	427 - 588	499 - 649	406 - 639	509 - 687	606 - 722	510 - 760	8 - 96	33 - 60	12 - 49
Present work	450 ± 1	485 ± 1	491 ± 1	543 ± 1	571 ± 10	605 ± 1	46 ± 2	40 ± 7	21 ± 4
CM material	255 - 310			535 - 620			30 - 50		
ASTM A240/A240M	170			485			40		

4. Discussion

MAM and especially SLM studied in this work, produce parts with a unique microstructure which impacts the macroscopic behavior. In the case of tensile tests, the SLM 316L SS specimens tend to have higher YS than CM 316L SS, and equivalent UTS and ductility. This is explained by considering the microstructure with factors such as the presence of cellular dendritic structure, smaller grain size and higher dislocation density [4,15,42,60].

In this section, the results of the microstructural analysis and the mechanical tests are combined to discuss the influence of the SLM process on the mechanical response. First, the effect of strain rate sensitivity is considered. Then the discussion focuses on the influence of the building direction and ends with the study of the specimen thickness.

The effect of the loading rate is investigated on all the configurations and is quantified with the evolution of the mechanical properties. A positive strain rate sensitivity is noticed for all tensile specimens. Considering $\sigma_{0.05}$ and UTS, there is an average increase of respectively 11±1% and 9±1% between the three lower strain rates for all configurations. The increase of the flow stress along with the strain rate is caused by multiple factors such as the dislocation multiplication and the twin nucleation and growth [61]. A gap of the flow stress between 0.067 and 8 s^{-1} strain rates is noticeable on the true

stress-strain curves of Bd90_t075, Bd90_t1 and Bd0_t1. The results of Li et al. [5] also show a gap between 0.54 and 193 s^{-1} strain rates for vertical specimens with a 1 mm thickness. This transition strain rate seems to tend toward a threshold value of 1 s^{-1}, as a result of a change in the deformation mechanisms [62]. Thus, the present work provides a more precise range of strain rates for this transition phase.

To quantify the dependence of the stress on the strain rate, the strain rate sensitivity, expressed by m, is frequently calculated at a given strain and temperature with the following equation [6,10,22,23] :

$$m = \frac{\partial \ln \sigma}{\partial \dot{\varepsilon}} \tag{3}$$

with σ the tensile stress and $\dot{\varepsilon}$ the strain rate. σ can be considered either as the YS [22], the UTS [23] or an engineering stress for a fixed strain, for instance 0.04 as used in [10]. Obviously, the choice of the tensile stress influences the m value. Thus, in this work, two different flow stresses are considered : engineering stress for a strain value of 0.05 ($\sigma_{0.05}$) and UTS. The plots of the two m values, and the associated results are presented in **Fig. 13**. For Bd90, it is the combination of the results of Bd90_t1 and Bd90_t15. This hypothesis is validated by the work of Wang et al. [12] who noticed that the mechanical properties become steady for thicknesses of 1 mm and higher. From the curves of **Fig. 13**a,b, it can be concluded that there is no strain rate sensitivity for Bd90_t05. For both $\sigma_{0.05}$ and UTS, the highest strain rate sensitivities are observed for horizontal and vertical specimens with a minimum thickness of 1 mm and the lowest for Bd90_t075 and Bd45_t1. Also, the sensitivity is greater when considering $\sigma_{0.05}$ rather than UTS. It is explained by a threshold strain of 10% from which the twinning induced plasticity lowers the increase of the flow stress [63]. With $m_{UTS} = 0.0061$, the CM 316L SS has a lower strain rate sensitivity than the SLM material [23]. This is explained by a refinement of the grain structure, as discussed previously. In the literature [22,23], only horizontal specimens are considered and similar m values are obtained. This study allows to consider the evolution of the three BD and thicknesses with the strain rate and two distinct tensile stresses.

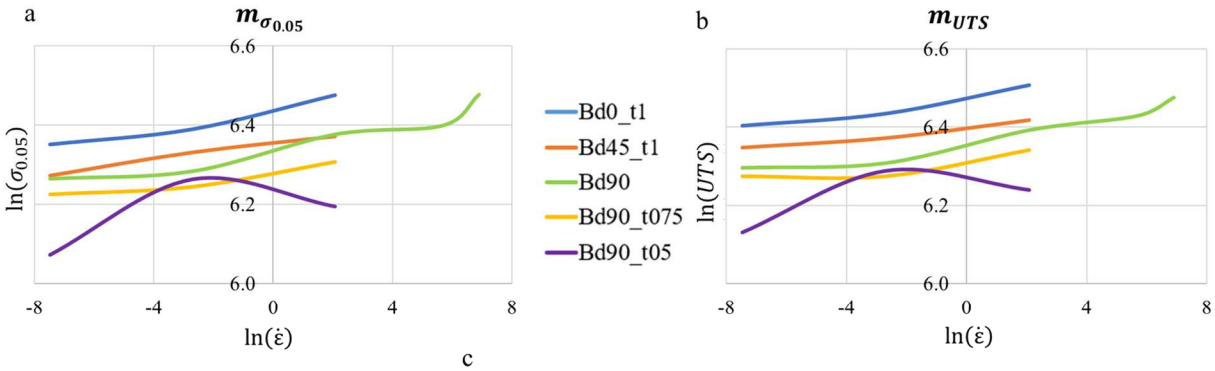

c

Configuration	*m* value	
	$\sigma_{0.05}$	UTS
Bd0_t1	0.013	0.011
Bd45_t1	0.010	0.007
Bd90	0.014	0.012
Bd90_t1	0.012	0.010
Bd90_t075	0.009	0.007

Fig. 13. Strain rate sensitivity : curves of (a) $m_{\sigma_{0.05}}$ and (b) m_{UTS} ; (c) table resuming the m values.

The increase in strain rates for a range of 10^{-3} to 10^{3} s^{-1} results in an enhancement of the flow stress, between 19.6% and 23.7% for the considered mechanical parameters. A threshold strain rate of 1 s^{-1} from which the increase of flow stress changes suddenly appears for certain configurations due to a change in the deformation mechanisms. Thus, the 316L SS produced by SLM is sensitive to the increase of strain rate, and in particular more than the CM material.

The mechanical results of the three BD at each strain rate and the microstructure analysis are associated to understand the effect of the process on the mechanical response. True stress-strain curves of the three BD for 1 mm thickness specimens at each strain rates are shown in **Fig. 14**a-c. Bd0 has the highest $\sigma_{0.05}$ and UTS but the lowest failure strain whereas it is the opposite for Bd90. The microstructure of the latter is composed of columnar grains oriented in the TD with <001> fiber texture, so dislocations have fewer boundaries to cross than for the microstructure of Bd0_t1 with narrow and elongated grains perpendicular to the TD. It results in higher flow stress for Bd0_t1 [43]. The SEM images presented in **Fig. 15** highlight a more jagged fracture surface for Bd0_t1 than for Bd90_t1 specimens. Suryawanshi et al. [11] linked this observation to a reduction in the failure strain by considering that, in the case of horizontal specimens, the location of porosities in the interlayers induces a higher number of microcracks as they are aligned along the TD. The higher ductility of Bd90_t1 can be explained by the columnar grain structure oriented along the TD but also by the <001> fiber texture [64]. The mechanical parameters of the diagonal specimens fall in the range of the two other BD. Considering the true stress-strain curves, the behavior of Bd45_t1 is closer to Bd90_t1. It is confirmed by the microstructures with more similarities between the two previous ones compared to horizontal specimens. This is due to comparable cooling kinetics for vertical and diagonal configurations with 1 mm and 1.4 mm scan lengths, respectively, compared to the 130 mm of the horizontal one. Considering a smaller scale, a similar hardness is achieved by the three-building orientations, proof that at the grain scale, there is no anisotropy. The morphology of the grains and the crystalline texture are responsible for the anisotropy observed at the macroscopic scale.

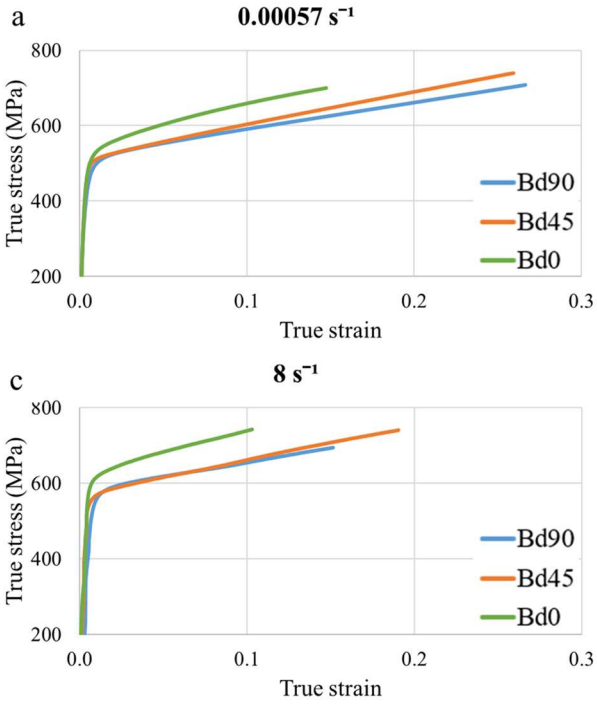

d

	Lankford ratios		
	r_0	r_{45}	r_{90}
This work	0.71 ± 0.06	1.05 ± 0.04	0.42 ± 0.05
Li et al [5]	0.97	0.92	0.83
Tancogne-Dejean et al [21]	0.81 ± 0.11		1.04 ± 0.11

Fig. 14. True stress-strain curves of 1 mm thick samples with the three BD at strain rates of (a) 0.00057 s^{-1}, (b) 0.067 s^{-1} and (c) 8 s^{-1}; (d) table of the Lankford ratios *r* of the three BD of this work and two others [5,21].

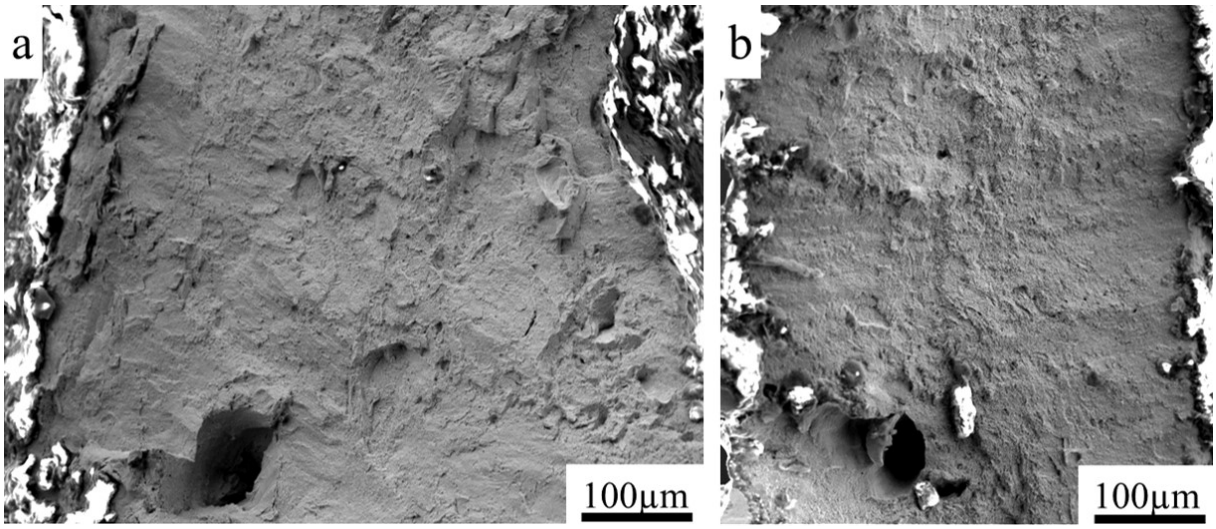

Fig. 15. SEM images of the fracture surfaces of (a) Bd0_t1 and (b) Bd90_t1.

Another way to quantify the building orientation sensitivity is to consider the Lankford ratio *r*. They are determined from the slope of the true plastic width strain over the true plastic through-thickness strain (which is computed from the axis and width strain measurements assuming plastic incompressibility) at the lowest strain rate. The variation of the Lankford ratios from 0.42 to 1.05 observed in **Fig. 14**d clearly indicates an anisotropy of the material. Diagonal specimens have the most homogenous grain structure, which can explain the Lankord ratio of 1 with a similar true plastic strain along the width and through the thickness. On the other hand, with elongated grains parallel to the BD, the true plastic strain is much higher along the axis and thus through the thickness (considering the plastic incompressibility) than along the width, causing a ratio inferior to 0.5. The horizontal specimen has grains oriented along the width, and thus, as the failure strain is lower for this orientation compared to others, the ratio of the true plastic strain is inferior to 1 but higher than 0.5. Li et al. [5] observed a minor anisotropy for the three BD with Lankford coefficients in the range of 0.8 - 1. Tancogne-Dejean et al. [21] noticed a lower difference between horizontal (0.81) and vertical (1.04) specimens. Unlike the other works, there is a large scatter of the Lankford ratios over the three BD caused by the various microstructures in this study. The main distinction with the two mentioned studies is that their specimens are cut in the middle of the same 1 mm thick wall. It results in less important distinctions in the grain structure along the different BD with no influence of the free edges on the specimens of [5,21]. In the present work, no machining is realized in order consider this phenomenon and to be as representative of the process as possible.

The analysis of the *m* value shows a similar strain rate sensitivity for horizontal and vertical specimens whereas diagonal ones are less sensitive. This orientation has a more homogeneous microstructure with no preferred crystallographic orientation compared to the two others, thereby explaining the lower sensitivity of Bd45 specimens [23]. The average maximal variations of $\sigma_{0.05}$ and UTS measured between the three BD are respectively 13±1% and 14±1% for the three lowest strain rates, with a nearly constant evolution between each BD. Thus, it shows that the material anisotropy is not affected by the strain rate. For the SLM 316L SS, the material anisotropy is only investigated for quasi-static loading. At a strain rate of 0.001 s^{-1}, Li et al. [5] noticed a similar variation of ±10% for the YS between the same BD and concluded to an anisotropic behavior. The CM material, investigated by Ghosh and Gurao et al. [65], has differences among the three BD of 3% for the YS under a quasi-static loading. These lower anisotropy can be explained by the more equiaxed and uniform grain structure compared to the SLM material [4].

The differences in grain morphology and texture on the microstructure between the three BD generates distinct macroscopic mechanical responses. This anisotropy in the mechanical behavior is accentuated by the edge effects induced by the process and is insensitive to the strain rate for a range of 0.00057 to

8 s^{-1}. The distinct strain rate sensitivities are also a consequence of the differences in grain morphology and texture.

The comparison between the three thicknesses allows to estimate the capacity of the SLM process to produce very thin specimens with convenient mechanical properties. First, it is important to specify the influence of the thermal treatment on Bd90_t1, as the two other thicknesses are not treated in order not to damage the geometry of the specimens. The heat treatment can result in a relatively higher failure strain but reduced tensile stress due to microstructural evolution characterized by a reduction of the texture and/or an increase of the grain size [48,66]. With a similar heat treatment, Saeidi et al. [67] noticed reductions of 12% of the YS and 7% of the UTS. Thus, lower YS and UTS and higher failure strain can be expected for the thicknesses of 0.5 and 0.75 mm in the case where they were thermally treated.

In **Fig. 16**, the true stress-train curves of 0.5 - 0.75 – 1 mm thicknesses vertically built samples are plotted for the three slowest strain rates. Bd90_t05 specimens have the lower flow stress in each case. There is a respective increase of 14% and 16% of the YS and UTS at a strain rate of 0.00057 s^{-1} from 0.5 to 1 mm thickness. Compared to the CM material and the standards of ASTM A240 [68], Bd90_t05 does not satisfy the requirements whereas from a thickness of 0.75 mm, the requirements are largely reached. Thus, in the case where Bd90_t075 is thermally treated, the standards of the norm will still be meeting as the marge of the as-built specimens is sufficient to compensate for the loss in the YS and UTS. Thus, in this study, a specimen thickness of 0.75 mm is the minimum value to be considered to obtain a satisfactory mechanical behavior.

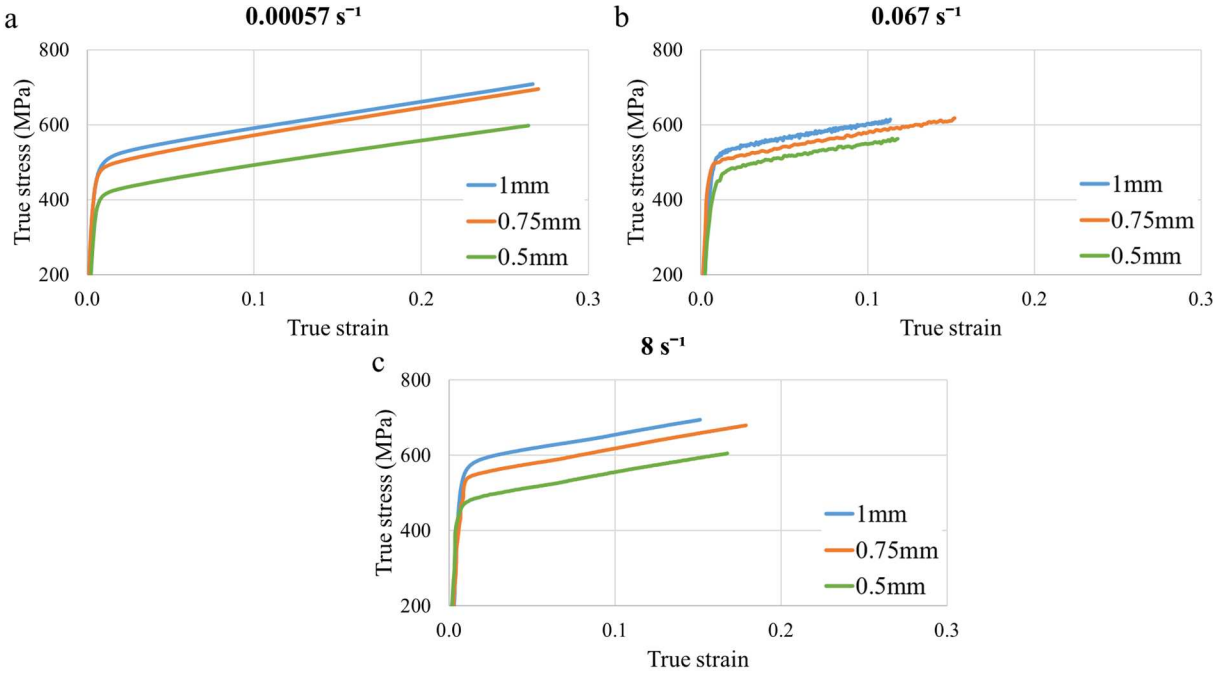

Fig. 16. True stress-strain curves of vertical samples (Bd90) with 0.5 - 0.75 – 1 mm thicknesses at strain rates of (a) 0.00057 s^{-1}, (b) 0.067 s^{-1} and (c) 8 s^{-1}.

Tancogne-Dejean et al. [8] linked the decreased mechanical properties with the decreasing thickness using microstructure explanations. It is caused by the different temperature history during manufacturing for each thickness resulting in distinct microstructures. As there is a huge thermal conductivity difference between the metal powder and the deposited bulk material [69], the higher the thickness, the higher amount of heat can be dissipated. There are few differences on the microstructures of Bd90_t075 and Bd90_t1 resulting in similar tensile flow stress. However, in the case of a lower thickness, Bd90_t05, there are more distinctions. The microstructure of the latter has a higher number of porosities, a more random texture and the grain morphology is more homogeneous compared to the two other thicknesses.

It results in a lower cohesion between successive layers and thus lower mechanical properties [32]. The similar hardness for Bd90_t05 and other configurations at the grain scale also confirms that the weaker behavior is caused by the lack of cohesion.

The strain rate sensitivity parameter *m* (**Fig. 13**) and the superposition of true stress-strain curves (**Fig. 16**) show different strain rate sensitivities for the three specimen thicknesses of 0.5 - 0.75 - 1 mm. The configurations Bd90_t1 and Bd90_t075 see a positive jump in their flow stress between strain rates from 0.067 to 8 s^{-1}. This higher *m* value of Bd90_t1 is explained by a more homogeneous microstructure than Bd90_t075. The Bd90_t05 configuration has a sensitivity that cannot be quantified in the same way as for the other two thicknesses. There is an increase of 21% for $\sigma_{0.05}$ for strain rates between 0.00057 and 0.067 s^{-1}, followed by a decrease of 7% between 0.067 and 8 s^{-1}. This variation is caused by a lower fabrication quality which is reflected in the microstructure with a higher amount of porosity and less cohesion between the layers.

A minimum thickness of 0.75 mm is sufficient, in this study, to obtain a mechanical response that meets the requirements of ASTM A240/A240M. For a thickness of 0.5 mm, the requirements of these same standards are not met due to a porous microstructure with a reduced cohesion between layers. This microstructure is responsible for an inconsistent strain rate sensitivity. This is not the case for the two other thicknesses, with comparable microstructures, which have similar positive strain rate sensitivities.

5. Conclusion

The influence of the build orientation and the thickness at multiple strain rates on the mechanical behavior of SLM 316L SS in the case of tensile tests is explored. Analysis of the microstructure combined with comparison with literature have allowed to understand the macroscopic results. The key outcomes drawn in this study are:

- SLM 316L SS achieves better YS, similar UTS and equal or lower failure strain compared to the CM material, except for Bd90_t05. The subgrain structure, the morphology of grains and higher density dislocation specific to SLM process are mainly responsible for this enhancement.
- The positive strain rate sensitivity corresponds to the range of values found in literature and is higher than the CM material. For strain rates ranging from 10^{-3} to 10^{3} s^{-1}, there is an increase of 24% of $\sigma_{0.05}$ and 20 % of UTS.
- Horizontal specimens have the highest tensile stress but the failure strain is nearly divided by two compared to the other BD. The microstructures show important differences in the morphology of the grain and the texture, resulting in the material anisotropy. Similar strain rate sensitivities are obtained for horizontal and vertical specimens with hierarchical and heterogenous grain structure. Diagonal specimens with homogenous microstructure are less sensitive to the strain rate.
- To ensure reliable mechanical properties, a minimum thickness of 0.75 mm is advised. At lower thickness, the requirements of the norm ASTM A240/A240M are not reached due to a microstructure characterized by a higher porosity and a weaker cohesion between layers. Also, as a consequence of the microstructure, the strain sensitivity is inconsistent for Bd90_t05 whereas it is higher for Bd90_t1 than for Bd90_t075.

Acknowledgements

The authors are grateful to Institut Carnot ARTS and Hauts-de-France Regional Council who funded this work.

References

[1] Hong Y, Zhou C, Zheng Y, Zhang L, Zheng J, Chen X, et al. Formation of strain-induced martensite in selective laser melting austenitic stainless steel. Mater Sci Eng A 2019;740–741:420–6. https://doi.org/10.1016/j.msea.2018.10.121.

[2] Bartolomeu F, Faria S, Carvalho O, Pinto E, Alves N, Silva FS, et al. Predictive models for physical and mechanical properties of Ti6Al4V produced by Selective Laser Melting. Mater Sci Eng A 2016;663:181–92. https://doi.org/10.1016/j.msea.2016.03.113.

[3] Tomus D, Tian Y, Rometsch PA, Heilmaier M, Wu X. Influence of post heat treatments on anisotropy of mechanical behaviour and microstructure of Hastelloy-X parts produced by selective laser melting. Mater Sci Eng A 2016;667:42–53. https://doi.org/10.1016/j.msea.2016.04.086.

[4] Röttger A, Geenen K, Windmann M, Binner F, Theisen W. Comparison of microstructure and mechanical properties of 316L austenitic steel processed by selective laser melting with hot-isostatic pressed and cast material. Mater Sci Eng A 2016;678:365–76. https://doi.org/10.1016/j.msea.2016.10.012.

[5] Li X, Roth CC, Tancogne-Dejean T, Mohr D. Rate- and temperature-dependent plasticity of additively manufactured stainless steel 316L: Characterization, modeling and application to crushing of shell-lattices. Int J Impact Eng 2020;145:103671. https://doi.org/10.1016/j.ijimpeng.2020.103671.

[6] Wang X, Liu Y, Shi T, Wang Y. Strain rate dependence of mechanical property in a selective laser melted 17–4 PH stainless steel with different states. Mater Sci Eng A 2020;792:139776. https://doi.org/10.1016/j.msea.2020.139776.

[7] Yap CY, Chua CK, Dong ZL, Liu ZH, Zhang DQ, Loh LE, et al. Review of selective laser melting: Materials and applications. Appl Phys Rev 2015;2:041101. https://doi.org/10.1063/1.4935926.

[8] Tancogne-Dejean T, Spierings AB, Mohr D. Additively-manufactured metallic micro-lattice materials for high specific energy absorption under static and dynamic loading. Acta Mater 2016;116:14–28. https://doi.org/10.1016/j.actamat.2016.05.054.

[9] AlMahri S, Santiago R, Lee D-W, Ramos H, Alabdouli H, Alteneiji M, et al. Evaluation of the dynamic response of triply periodic minimal surfaces subjected to high strain-rate compression. Addit Manuf 2021;46:102220. https://doi.org/10.1016/j.addma.2021.102220.

[10] Maconachie T, Leary M, Zhang J, Medvedev A, Sarker A, Ruan D, et al. Effect of build orientation on the quasi-static and dynamic response of SLM AlSi10Mg. Mater Sci Eng A 2020:139445. https://doi.org/10.1016/j.msea.2020.139445.

[11] Suryawanshi J, Prashanth KG, Ramamurty U. Mechanical behavior of selective laser melted 316L stainless steel. Mater Sci Eng A 2017;696:113–21. https://doi.org/10.1016/j.msea.2017.04.058.

[12] Wang X, Muñiz-Lerma JA, Sánchez-Mata O, Attarian Shandiz M, Brochu M. Microstructure and mechanical properties of stainless steel 316L vertical struts manufactured by laser powder bed fusion process. Mater Sci Eng A 2018;736:27–40. https://doi.org/10.1016/j.msea.2018.08.069.

[13] Saeidi K, Gao X, Zhong Y, Shen ZJ. Hardened austenite steel with columnar sub-grain structure formed by laser melting. Mater Sci Eng A 2015;625:221–9. https://doi.org/10.1016/j.msea.2014.12.018.

[14] Rankouhi B, Bertsch KM, Meric de Bellefon G, Thevamaran M, Thoma DJ, Suresh K. Experimental validation and microstructure characterization of topology optimized, additively manufactured SS316L components. Mater Sci Eng A 2020;776:139050. https://doi.org/10.1016/j.msea.2020.139050.

[15] Agrawal AK, Meric de Bellefon G, Thoma D. High-throughput experimentation for microstructural design in additively manufactured 316L stainless steel. Mater Sci Eng A 2020;793:139841. https://doi.org/10.1016/j.msea.2020.139841.

[16] Pham MS, Dovgyy B, Hooper PA. Twinning induced plasticity in austenitic stainless steel 316L made by additive manufacturing. Mater Sci Eng A 2017;704:102–11. https://doi.org/10.1016/j.msea.2017.07.082.

[17] Shrestha R, Simsiriwong J, Shamsaei N. Fatigue behavior of additive manufactured 316L stainless steel parts: Effects of layer orientation and surface roughness. Addit Manuf 2019;28:23–38. https://doi.org/10.1016/j.addma.2019.04.011.

[18] Tolosa I, Garciandía F, Zubiri F, Zapirain F, Esnaola A. Study of mechanical properties of AISI 316 stainless steel processed by "selective laser melting", following different manufacturing strategies. Int J Adv Manuf Technol 2010;51:639–47. https://doi.org/10.1007/s00170-010-2631-5.
[19] Song M, Wang M, Lou X, Rebak RB, Was GS. Radiation damage and irradiation-assisted stress corrosion cracking of additively manufactured 316L stainless steels. J Nucl Mater 2019;513:33–44. https://doi.org/10.1016/j.jnucmat.2018.10.044.
[20] Roach AM, White BC, Garland A, Jared BH, Carroll JD, Boyce BL. Size-dependent stochastic tensile properties in additively manufactured 316L stainless steel. Addit Manuf 2020;32:101090. https://doi.org/10.1016/j.addma.2020.101090.
[21] Tancogne-Dejean T, Gorji MB, Pack K, Roth CC. The third Sandia Fracture Challenge: deterministic and probabilistic modeling of ductile fracture of additively-manufactured material. Int J Fract 2019. https://doi.org/10.1007/s10704-019-00355-z.
[22] Li Z, Voisin T, McKeown JT, Ye J, Braun T, Kamath C, et al. Tensile properties, strain rate sensitivity, and activation volume of additively manufactured 316L stainless steels. Int J Plast 2019;120:395–410. https://doi.org/10.1016/j.ijplas.2019.05.009.
[23] Khodabakhshi F, Farshidianfar MH, Gerlich AP, Nosko M, Trembošová V, Khajepour A. Microstructure, strain-rate sensitivity, work hardening, and fracture behavior of laser additive manufactured austenitic and martensitic stainless steel structures. Mater Sci Eng A 2019;756:545–61. https://doi.org/10.1016/j.msea.2019.04.065.
[24] Charmi A, Falkenberg R, Ávila L, Mohr G, Sommer K, Ulbricht A, et al. Mechanical anisotropy of additively manufactured stainless steel 316L: An experimental and numerical study. Mater Sci Eng A 2021;799:140154. https://doi.org/10.1016/j.msea.2020.140154.
[25] Hitzler L, Hirsch J, Heine B, Merkel M, Hall W, Öchsner A. On the Anisotropic Mechanical Properties of Selective Laser-Melted Stainless Steel. Mater Basel Switz 2017;10. https://doi.org/10.3390/ma10101136.
[26] Wiesent L, Schultheiß U, Lulla P, Nonn A, Noster U. Mechanical properties of small structures built by selective laser melting 316 L stainless steel – a phenomenological approach to improve component design. Mater Werkst 2020;51:1615–29. https://doi.org/10.1002/mawe.202000038.
[27] Leicht A, Pauzon C, Rashidi M, Klement U, Nyborg L, Hryha E. Effect of part thickness on the microstructure and tensile properties of 316L parts produced by laser powder bed fusion. Adv Ind Manuf Eng 2021;2:100037. https://doi.org/10.1016/j.aime.2021.100037.
[28] Tsopanos S, Mines R a. W, McKown S, Shen Y, Cantwell WJ, Brooks W, et al. The Influence of Processing Parameters on the Mechanical Properties of Selectively Laser Melted Stainless Steel Microlattice Structures. J Manuf Sci Eng 2010;132. https://doi.org/10.1115/1.4001743.
[29] Gümrük R, Mines RAW, Karadeniz S. Determination of Strain Rate Sensitivity of Micro-struts Manufactured Using the Selective Laser Melting Method. J Mater Eng Perform 2018;27:1016–32. https://doi.org/10.1007/s11665-018-3208-y.
[30] Gümrük R, Mines RAW. Compressive behaviour of stainless steel micro-lattice structures. Int J Mech Sci 2013;68:125–39. https://doi.org/10.1016/j.ijmecsci.2013.01.006.
[31] Li P. Constitutive and failure behaviour in selective laser melted stainless steel for microlattice structures. Mater Sci Eng A 2015;622:114–20. https://doi.org/10.1016/j.msea.2014.11.028.
[32] Leicht A, Klement U, Hryha E. Effect of build geometry on the microstructural development of 316L parts produced by additive manufacturing. Mater Charact 2018;143:137–43. https://doi.org/10.1016/j.matchar.2018.04.040.
[33] Liverani E, Toschi S, Ceschini L, Fortunato A. Effect of selective laser melting (SLM) process parameters on microstructure and mechanical properties of 316L austenitic stainless steel. J Mater Process Technol 2017;249:255–63. https://doi.org/10.1016/j.jmatprotec.2017.05.042.
[34] ASTM E384-17. Standard Test Method for Microindentation Hardness of Materials. n.d.
[35] Carrier J, Markiewicz E, Haugou G, Lebaillif D, Leconte N, Naceur H. Influence of the heat affected zone on the dynamic behavior of a welded joint of armoured steel. Int J Impact Eng 2017;104:154–63. https://doi.org/10.1016/j.ijimpeng.2016.12.022.
[36] Gong H, Rafi K, Gu H, Janaki Ram GD, Starr T, Stucker B. Influence of defects on mechanical properties of Ti–6Al–4V components produced by selective laser melting and electron beam melting. Mater Des 2015;86:545–54. https://doi.org/10.1016/j.matdes.2015.07.147.

[37] Larimian T, Kannan M, Grzesiak D, AlMangour B, Borkar T. Effect of energy density and scanning strategy on densification, microstructure and mechanical properties of 316L stainless steel processed via selective laser melting. Mater Sci Eng A 2020;770:138455. https://doi.org/10.1016/j.msea.2019.138455.
[38] Li C, White R, Fang XY, Weaver M, Guo YB. Microstructure evolution characteristics of Inconel 625 alloy from selective laser melting to heat treatment. Mater Sci Eng A 2017;705:20–31. https://doi.org/10.1016/j.msea.2017.08.058.
[39] DebRoy T, Wei HL, Zuback JS, Mukherjee T, Elmer JW, Milewski JO, et al. Additive manufacturing of metallic components – Process, structure and properties. Prog Mater Sci 2018;92:112–224. https://doi.org/10.1016/j.pmatsci.2017.10.001.
[40] King WE, Barth HD, Castillo VM, Gallegos GF, Gibbs JW, Hahn DE, et al. Observation of keyhole-mode laser melting in laser powder-bed fusion additive manufacturing. J Mater Process Technol 2014;214:2915–25. https://doi.org/10.1016/j.jmatprotec.2014.06.005.
[41] Bansal GK, Chandan AK, Srivastava VC, Krishna KG, Das G, Rajkumar S, et al. Studies on Tensile Behaviour of Selective Laser Melted 316L Stainless Steel Using SEM Straining Stage. Trans Indian Natl Acad Eng 2021. https://doi.org/10.1007/s41403-021-00214-1.
[42] Chniouel A, Giroux P-F, Lomello F, Aubry P, Vasquez É, Hercher O, et al. Influence of substrate temperature on microstructural and mechanical properties of 316L stainless steel consolidated by laser powder bed fusion. Int J Adv Manuf Technol 2020;111:3489–503. https://doi.org/10.1007/s00170-020-06316-4.
[43] Balit Y, Charkaluk E, Constantinescu A. Digital image correlation for microstructural analysis of deformation pattern in additively manufactured 316L thin walls. Addit Manuf 2020;31:100862. https://doi.org/10.1016/j.addma.2019.100862.
[44] Casati R, Lemke J, Vedani M. Microstructure and Fracture Behavior of 316L Austenitic Stainless Steel Produced by Selective Laser Melting. J Mater Sci Technol 2016;32:738–44. https://doi.org/10.1016/j.jmst.2016.06.016.
[45] Andreau O, Koutiri I, Peyre P, Penot J-D, Saintier N, Pessard E, et al. Texture control of 316L parts by modulation of the melt pool morphology in selective laser melting. J Mater Process Technol 2019;264:21–31. https://doi.org/10.1016/j.jmatprotec.2018.08.049.
[46] Niendorf T, Leuders S, Riemer A, Richard HA, Tröster T, Schwarze D. Highly Anisotropic Steel Processed by Selective Laser Melting. Metall Mater Trans B 2013;44:794–6. https://doi.org/10.1007/s11663-013-9875-z.
[47] Sun S-H, Ishimoto T, Hagihara K, Tsutsumi Y, Hanawa T, Nakano T. Excellent mechanical and corrosion properties of austenitic stainless steel with a unique crystallographic lamellar microstructure via selective laser melting. Scr Mater 2019;159:89–93. https://doi.org/10.1016/j.scriptamat.2018.09.017.
[48] Salman OO, Gammer C, Chaubey AK, Eckert J, Scudino S. Effect of heat treatment on microstructure and mechanical properties of 316L steel synthesized by selective laser melting. Mater Sci Eng A 2019;748:205–12. https://doi.org/10.1016/j.msea.2019.01.110.
[49] Puichaud A-H, Flament C, Chniouel A, Lomello F, Rouesne E, Giroux P-F, et al. Microstructure and mechanical properties relationship of additively manufactured 316L stainless steel by selective laser melting. EPJ Nucl Sci Technol 2019;5:23. https://doi.org/10.1051/epjn/2019051.
[50] Zhang Z, Chu B, Wang L, Lu Z. Comprehensive effects of placement orientation and scanning angle on mechanical properties and behavior of 316L stainless steel based on the selective laser melting process. J Alloys Compd 2019;791:166–75. https://doi.org/10.1016/j.jallcom.2019.03.082.
[51] Cherry JA, Davies HM, Mehmood S, Lavery NP, Brown SGR, Sienz J. Investigation into the effect of process parameters on microstructural and physical properties of 316L stainless steel parts by selective laser melting. Int J Adv Manuf Technol 2015;76:869–79. https://doi.org/10.1007/s00170-014-6297-2.
[52] Bartolomeu F, Buciumeanu M, Pinto E, Alves N, Carvalho O, Silva FS, et al. 316L stainless steel mechanical and tribological behavior—A comparison between selective laser melting, hot pressing and conventional casting. Addit Manuf 2017;16:81–9. https://doi.org/10.1016/j.addma.2017.05.007.

[53] ASTM E8/E8M. Standard Test Methods for Tension Testing of Metallic Materials n.d. https://www.astm.org/e0008_e0008m-21.html (accessed December 3, 2021).
[54] Barkia B, Aubry P, Haghi-Ashtiani P, Auger T, Gosmain L, Schuster F, et al. On the origin of the high tensile strength and ductility of additively manufactured 316L stainless steel: Multiscale investigation. J Mater Sci Technol 2020;41:209–18. https://doi.org/10.1016/j.jmst.2019.09.017.
[55] ASTM A240/A240M. Standard Specification for Chromium and Chromium-Nickel Stainless Steel Plate, Sheet, and Strip for Pressure Vessels and for General Applications. n.d.
[56] Wang X, Muñiz-Lerma JA, Attarian Shandiz M, Sanchez-Mata O, Brochu M. Crystallographic-orientation-dependent tensile behaviours of stainless steel 316L fabricated by laser powder bed fusion. Mater Sci Eng A 2019;766:138395. https://doi.org/10.1016/j.msea.2019.138395.
[57] Shamsujjoha Md, Agnew SR, Fitz-Gerald JM, Moore WR, Newman TA. High Strength and Ductility of Additively Manufactured 316L Stainless Steel Explained. Metall Mater Trans A 2018;49:3011–27. https://doi.org/10.1007/s11661-018-4607-2.
[58] Kurzynowski T, Gruber K, Stopyra W, Kuźnicka B, Chlebus E. Correlation between process parameters, microstructure and properties of 316 L stainless steel processed by selective laser melting. Mater Sci Eng A 2018;718:64–73. https://doi.org/10.1016/j.msea.2018.01.103.
[59] Gu D, Chen H. Selective laser melting of high strength and toughness stainless steel parts: The roles of laser hatch style and part placement strategy. Mater Sci Eng A 2018;725:419–27. https://doi.org/10.1016/j.msea.2018.04.046.
[60] Yin YJ, Sun JQ, Guo J, Kan XF, Yang DC. Mechanism of high yield strength and yield ratio of 316 L stainless steel by additive manufacturing. Mater Sci Eng A 2019;744:773–7. https://doi.org/10.1016/j.msea.2018.12.092.
[61] Lee W-S, Chen T-H, Lin C-F, Luo W-Z. Impact Response and Microstructural Evolution of 316L Stainless Steel under Ambient and Elevated Temperature Conditions. Metall Mater Trans A 2012;43:3998–4005. https://doi.org/10.1007/s11661-012-1233-2.
[62] Lee W-S, Lin C-F, Liu T-J. Strain rate dependence of impact properties of sintered 316L stainless steel. J Nucl Mater 2006;359:247–57. https://doi.org/10.1016/j.jnucmat.2006.09.003.
[63] Chen J, Wei H, Bao K, Zhang X, Cao Y, Peng Y, et al. Dynamic mechanical properties of 316L stainless steel fabricated by an additive manufacturing process. J Mater Res Technol 2021;11:170–9. https://doi.org/10.1016/j.jmrt.2020.12.097.
[64] Güden M, Yavaş H, Tanrıkulu AA, Taşdemirci A, Akın B, Enser S, et al. Orientation dependent tensile properties of a selective-laser-melt 316L stainless steel. Mater Sci Eng A 2021;824:141808. https://doi.org/10.1016/j.msea.2021.141808.
[65] Ghosh A, Gurao NP. Effect of crystallographic texture on the planar anisotropy of ratcheting response in 316 stainless steel sheet. Mater Des 2016;109:186–96. https://doi.org/10.1016/j.matdes.2016.07.079.
[66] Shin W-S, Son B, Song W, Sohn H, Jang H, Kim Y-J, et al. Heat treatment effect on the microstructure, mechanical properties, and wear behaviors of stainless steel 316L prepared via selective laser melting. Mater Sci Eng A 2021;806:140805. https://doi.org/10.1016/j.msea.2021.140805.
[67] Saeidi K, Gao X, Lofaj F, Kvetková L, Shen ZJ. Transformation of austenite to duplex austenite-ferrite assembly in annealed stainless steel 316L consolidated by laser melting. J Alloys Compd 2015;633:463–9. https://doi.org/10.1016/j.jallcom.2015.01.249.
[68] A01 Committee. Specification for Chromium and Chromium-Nickel Stainless Steel Plate, Sheet, and Strip for Pressure Vessels and for General Applications. ASTM International; n.d. https://doi.org/10.1520/A0240_A0240M-20A.
[69] Raghavan N, Dehoff R, Pannala S, Simunovic S, Kirka M, Turner J, et al. Numerical modeling of heat-transfer and the influence of process parameters on tailoring the grain morphology of IN718 in electron beam additive manufacturing. Acta Mater 2016;112:303–14. https://doi.org/10.1016/j.actamat.2016.03.063.